Phase-Locked Loop Based on an Observer for Grid Synchronization

Yongsoon Park, *Student Member, IEEE*, Seung-Ki Sul, *Fellow, IEEE*, Woo-Chull Kim, and Hyun-Young Lee

***Abstract*—A grid synchronization technique is essential for grid-connected power converters. Phase-locked loop (PLL) has been widely exploited as an implementation technique, but additional efforts are required to deal with severely distorted grid voltages. In this paper, an observer is proposed to enhance the performance of PLL. A state equation is newly formulated to construct the observer, which extracts positive-sequence voltage from the distorted grid voltage. Additionally, guidelines are suggested to set the observer gains by considering its internal transfer functions. The PLL and proposed observer have been tested in simulations and experiments in contrast to dual second-order generalized integrator frequency-locked loop. The results have shown that the proposed method reveals a better phase-tracking performance for grid synchronization.**

***Index Terms*—Digital signal processing, grid synchronization, grid-tied converter, observer, phase-locked loop (PLL), positive-sequence voltage.**

I. Introduction

ELECTRICITY is delivered from suppliers to consumers via an electrical grid. The grid voltage is expected to be sinusoidal, whose frequency is fundamentally 50 or 60 Hz. This normal voltage is called a positive-sequence voltage. In particular, electrical power is mainly transferred by modulating the ac current corresponding to the positive-sequence voltage, and it is useful to separate this from the rest of the "apparent power" [1].

The grid voltage phase angle should be detected to elaborately modulate active and reactive powers when a grid-connected converter participates in power delivery. For this purpose, the method based on phase-locked loop (PLL) in the synchronous reference frame (SRF-PLL) has been widely used [2], [3]. However, since the grid voltage is usually polluted by unexpected distortions such as harmonics, unbalances, and glitches, the detection of its phase angle may not be easy with the simple PLL method.

Manuscript received April 25, 2013; revised July 3, 2013; accepted August 2, 2013. Date of publication August 21, 2013; date of current version March 17, 2014. Paper 2013-SECSC-194.R1, presented at the 2013 IEEE Applied Power Electronics Conference and Exposition, Long Beach, CA, USA, March 17–21, and approved for publication in the IEEE TRANSACTIONS ON INDUSTRY APPLICATIONS by the Sustainable Energy Conversion Systems Committee of the IEEE Industry Applications Society.

Y. Park and S.-K. Sul are with Seoul National University, Seoul 151-742, Korea (e-mail: yongsoon@eepel.snu.ac.kr; sulsk@plaza.snu.ac.kr).

W.-C. Kim is with LG Uplus Corporation, Seoul 121-270, Korea (e-mail: charles@lguplus.co.kr).

H.-Y. Lee is with PLASPO Company, Ltd., Goyang City 410-722, Korea (e-mail: withlhy@plaspo.co.kr).

Color versions of one or more of the figures in this paper are available online at http://ieeexplore.ieee.org.

Digital Object Identifier 10.1109/TIA.2013.2279194

Therefore, many attempts have been made to enhance the detection performance under polluted grid conditions [4]–[15]. When the recent research studies are considered, a better method for grid synchronization is to fulfill the following requirements simultaneously. First, the mitigation of unbalance and harmonics should be achieved under higher dynamics to track the phase angle variation. Second, the consistency of grid synchronization has to be guaranteed even if grid frequency varies.

In general, each required function can be implemented in several stages with filter-type blocks [4]–[9]. In some cases, the implementation can be based on parallel structure [12], [13]. Even if all of these methods have already presented effective performances in functional aspects, the computational efficiency is not high due to the distributed structures. Moreover, the integrated system design becomes more complicated when the number of separate parts increases. By using a specialized filter, the rejection at every harmonic has been attempted with the relatively simple structure [14], [15]. However, this method should save the previously sampled values, and its sampling frequency must be set carefully in conjunction with the grid frequency. Therefore, an appropriate compromise is required between the implementation effort and the grid synchronization performance.

In this paper, an observer is proposed to clearly extract the positive-sequence component of the grid voltage. The required functions for grid synchronization can be unified into a single observer by virtue of its state equation, which has been newly derived in this paper. As a result, the proposed method has a relatively simple structure while presenting the phase detection performance comparable to the dual second-order generalized integrator frequency-locked loop (DSOGI-FLL) [10].

In terms of design and analysis, the following points can be further noted: although the observer gains are generally set on the basis of the heuristic insight of the designer, this paper suggests explicit guidelines in setting the gains considering the internal transfer functions. In addition, the analyzing tools are newly introduced to discuss the unified effect of the proposed fourth-order observer and to examine the distortions from digital implementation.

The organization of this paper is as follows. In Section II, how the observer can extract positive-sequence voltage with less distortion is described. After the observer gains are set, the observer to PLL attachment is detailed in Section III. The proposed method is then assessed via simulation and experimental results under grid fault situations in Section IV. Finally, concluding remarks are noted in Section V.

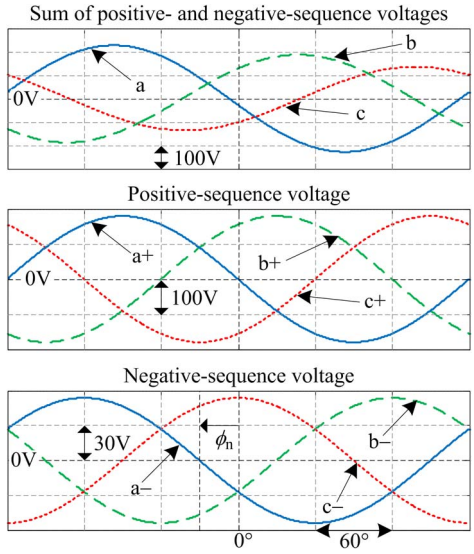

Fig. 1. Positive- and negative-sequence voltages.

II. Extraction of Positive-Sequence Voltages

A. Definitions of Symmetrical Components

In general, the three-phase voltage can be decomposed into symmetrical components: positive-, negative-, and zero-sequence voltages [18]. Among them, negative-sequence voltage arises mainly when the grid is under abnormal operating conditions such as phase-to-ground faults and unbalanced loading conditions. In SRF-PLL, it is hard to filter out the negative-sequence voltage in the SRF even though the bandwidth of PLL is quite reduced. [3], [4]. To effectively remove the negative-sequence voltage, the symmetrical component modeling can be considered.

Initially, the positive-sequence voltage can be defined as

$$\begin{cases} v_{a+} = -V_+ \sin\theta_p \\ v_{b+} = -V_+ \sin(\theta_p - 120^\circ) \\ v_{c+} = -V_+ \sin(\theta_p + 120^\circ) \end{cases} \tag{1}$$

where both subscripts "+" and "p" refer to the positive sequence and θ_p is the phase angle of the positive-sequence voltage.

As per the definition of (1), the positive-sequence voltage only exists in the quadrature axis of the SRF. This definition has been adopted to maintain the coherence between grid and ac motor applications. By using the same phase angle in (1), the negative-sequence voltage can then be generalized into

$$\begin{cases} v_{a-} = -V_- \sin(\theta_p + \phi_n) \\ v_{b-} = -V_- \sin(\theta_p + \phi_n + 120^\circ) \\ v_{c-} = -V_- \sin(\theta_p + \phi_n - 120^\circ) \end{cases} \tag{2}$$

where the subscript "−" represents the negative sequence and ϕ_n is the phase difference of the negative-sequence voltage to the positive-sequence voltage.

For example, each voltage in (1) and (2) can be depicted in terms of the phase angle as shown in Fig. 1. In the figure, V_+ in (1) was set to 179.6 V, and V_- in (2) was 30% of V_+. In addition, ϕ_n in (2) was set to 30°. The sum of the positive- and negative-sequence voltages presents an unbalance as shown in Fig. 1.

B. Observer for Estimating Positive-Sequence Voltage

For the observer design, the state equation on grid voltage must first be established. This state equation explains the relationship between states and their derivatives. In essence, the grid voltage should be discussed in terms of its time variation. In particular, the grid voltage can be considered in the SRF by

$$\begin{bmatrix} v_d \\ v_q \end{bmatrix} = \frac{2}{3} \begin{bmatrix} \cos\hat{\theta}_p & \cos(\hat{\theta}_p - 120^\circ) & \cos(\hat{\theta}_p + 120^\circ) \\ -\sin\hat{\theta}_p & -\sin(\hat{\theta}_p - 120^\circ) & -\sin(\hat{\theta}_p + 120^\circ) \end{bmatrix} \times \begin{bmatrix} v_a \\ v_b \\ v_c \end{bmatrix} \tag{3}$$

where the hat "^" hereafter refers to estimated value.

For each phase, the sum of (1) and (2) can be inserted into the right side of (3). The zero-sequence voltage is not considered because it is naturally erased in the process of (3). The $d-q$ voltages can also be decomposed into positive- and negative-sequence components in the SRF

$$\begin{aligned} \begin{bmatrix} v_d \\ v_q \end{bmatrix} &= \begin{bmatrix} v_{d+} \\ v_{q+} \end{bmatrix} + \begin{bmatrix} v_{d-} \\ v_{q-} \end{bmatrix} \\ &= \begin{bmatrix} -V_+ \sin\theta_d \\ V_+ \cos\theta_d \end{bmatrix} + \begin{bmatrix} -V_- \sin(2\hat{\theta}_p + \theta_d + \phi_n) \\ -V_- \cos(2\hat{\theta}_p + \theta_d + \phi_n) \end{bmatrix} \end{aligned} \tag{4}$$

where

$$\theta_d = \theta_p - \hat{\theta}_p. \tag{5}$$

If $d\theta_d/dt$ and $d\phi_n/dt$ are negligible under the assumption of slow variation in the estimation error and phase difference, the derivative of (4) can be approximated by the chain rule into

$$\frac{d}{dt}\begin{bmatrix} v_d \\ v_q \end{bmatrix} \approx \frac{d}{dt}\begin{bmatrix} v_{d-} \\ v_{q-} \end{bmatrix} = 2\frac{d}{dt}\hat{\theta}_p \cdot \begin{bmatrix} -V_- \cos(2\hat{\theta}_p + \theta_d + \phi_n) \\ V_- \sin(2\hat{\theta}_p + \theta_d + \phi_n) \end{bmatrix}. \tag{6}$$

Each negative-sequence component in (4) is repeated in the other axis in (6). Equation (6) is then rearranged into

$$\frac{d}{dt}\begin{bmatrix} v_d \\ v_q \end{bmatrix} \approx 2\frac{d}{dt}\hat{\theta}_p \cdot \begin{bmatrix} v_{q-} \\ -v_{d-} \end{bmatrix} = 2\hat{\omega}_p \begin{bmatrix} v_q - v_{q+} \\ v_{d+} - v_d \end{bmatrix} \tag{7}$$

where ω is the angular frequency.

The novel derivation of (7) has led to the proposal of this paper. In (7), the derivatives of v_d and v_q can be explained with respect to themselves and the positive-sequence voltage (without the negative-sequence voltage). Furthermore, because it has been assumed that $d\theta_d/dt$ is small enough to derive (7), the derivative of the positive-sequence voltage in (4) can be

regarded as null. Then, the entire state equation of the grid voltage can be derived as

$$\frac{d}{dt}V_s = \begin{bmatrix} 0 & 2\hat{\omega}_p & 0 & -2\hat{\omega}_p \\ -2\hat{\omega}_p & 0 & 2\hat{\omega}_p & 0 \\ 0 & 0 & 0 & 0 \\ 0 & 0 & 0 & 0 \end{bmatrix} V_s = A_m V_s \quad \text{(8-a)}$$

$$V_o = \begin{bmatrix} v_d \\ v_q \end{bmatrix} = \begin{bmatrix} 1 & 0 & 0 & 0 \\ 0 & 1 & 0 & 0 \end{bmatrix} V_s = C_m V_s \quad \text{(8-b)}$$

$$V_s = [\, v_d \quad v_q \quad v_{d+} \quad v_{q+} \,]^{\mathrm{T}} \quad \text{(8-c)}$$

where the subscripts "s" and "o" refer to state and output, respectively.

A Luenberger observer can be designed as in (9) because the system is observable with A_m and C_m in (8) [16]

$$\frac{d}{dt}\hat{V}_s = A_m \hat{V}_s + L_m \cdot [V_o - C_m \hat{V}_s] \quad \text{(9-a)}$$

$$L_m = \begin{bmatrix} p_1 & p_3 & q_1 & q_3 \\ p_2 & p_4 & q_2 & q_4 \end{bmatrix}^{\mathrm{T}} \quad \text{(9-b)}$$

$$\hat{V}_s = [\, \hat{v}_d \quad \hat{v}_q \quad \hat{v}_{d+} \quad \hat{v}_{q+} \,]^{\mathrm{T}} \quad \text{(9-c)}$$

where variables in L_m are observer gains.

By virtue of the practical assumption on positive-sequence voltage, the observer in (9) could be newly proposed, which can observe the positive-sequence voltage in its internal state.

C. Gain Settings for the Observer

The observer gains of L_m in (9) must be specified. In general, it is difficult to logically describe why a set of observer gains has to be selected since certain selections may have to rely on the insight of the designer. In this paper, the gain setting of the observer is described with the reason why they are selected. The internal transfer functions of the observer are used to explain the gain setting. These functions can be derived as follows. Initially, the state equation in (9) can be transformed into (10) when the derivative operator is replaced with the Laplace operator

$$s \cdot \hat{V}_s = A_m \hat{V}_s + L_m \cdot [V_o - C_m \hat{V}_s]. \quad (10)$$

Equation (10) can be rearranged in terms of V_o

$$\hat{V}_s = [s \cdot I_m - A_m + L_m C_m]^{-1} \cdot L_m V_o \quad (11)$$

where I_m represents the identity matrix.

Hence, the estimated states in (9-c) can be expressed with respect to the measurable states in (8-b)

$$\begin{cases} \hat{v}_d = A_t/P_t \cdot v_d + E_t/P_t \cdot v_q \\ \hat{v}_q = B_t/P_t \cdot v_d + F_t/P_t \cdot v_q \\ \hat{v}_{d+} = C_t/P_t \cdot v_d + G_t/P_t \cdot v_q \\ \hat{v}_{q+} = D_t/P_t \cdot v_d + H_t/P_t \cdot v_q \end{cases} \quad (12)$$

where all transfer functions in (12) are detailed with

$$\begin{aligned} A_t =& p_1 s^3 + \{2\hat{\omega}_p(p_3 - q_3) + p_1 p_4 - p_2 p_3\} s^2 \\ &+ 2\hat{\omega}_p(p_1 q_2 - p_2 q_1 + p_3 q_4 - p_4 q_3 + 2\hat{\omega}_p q_1)s \\ &+ 4\hat{\omega}_p^2(q_1 q_4 - q_2 q_3) \quad \text{(13-a)} \\ B_t =& p_3 s^3 + 2\hat{\omega}_p(q_1 - p_1)s^2 + 4\hat{\omega}_p^2 q_3 s \quad \text{(13-b)} \\ C_t =& q_1 s^3 + (p_4 q_1 - p_3 q_2)s^2 \\ &+ 2\hat{\omega}_p(p_1 q_2 - p_2 q_1 + 2\hat{\omega}_p q_1)s \\ &+ 4\hat{\omega}_p^2(q_1 q_4 - q_2 q_3) \quad \text{(13-c)} \\ D_t =& q_3 s^3 + (p_4 q_3 - p_3 q_4)s^2 \\ &+ 2\hat{\omega}_p \{q_3(q_2 - p_2) + q_4(p_1 - q_1) + 2\hat{\omega}_p q_3\} s \quad \text{(13-d)} \\ E_t =& p_2 s^3 + 2\hat{\omega}_p(p_4 - q_4)s^2 + 4\hat{\omega}_p^2 q_2 s \quad \text{(13-e)} \\ F_t =& p_4 s^3 + \{2\hat{\omega}_p(q_2 - p_2) + p_1 p_4 - p_2 p_3\} s^2 \\ &+ 2\hat{\omega}_p(p_1 q_2 - p_2 q_1 + p_3 q_4 - p_4 q_3 + 2\hat{\omega}_p q_4)s \\ &+ 4\hat{\omega}_p^2(q_1 q_4 - q_2 q_3) \quad \text{(13-f)} \\ G_t =& q_2 s^3 + (p_1 q_2 - p_2 q_1)s^2 \\ &+ 2\hat{\omega}_p\{q_2(p_3 - q_3) + q_1(q_4 - p_4) + 2\hat{\omega}_p q_2\}s \quad \text{(13-g)} \\ H_t =& q_4 s^3 + (p_1 q_4 - p_2 q_3)s^2 \\ &+ 2\hat{\omega}_p(p_3 q_4 - p_4 q_3 + 2\hat{\omega}_p q_4)s \\ &+ 4\hat{\omega}_p^2(q_1 q_4 - q_2 q_3) \quad \text{(13-h)} \\ P_t =& \det[s \cdot I_m - A_m + L_m C_m] \\ =& s^4 + (p_1 + p_4)s^3 + 4\hat{\omega}_p^2(q_1 q_4 - q_2 q_3) \\ &+ \left\{4\hat{\omega}_p^2 + 2\hat{\omega}_p(p_3 - p_2 + q_2 - q_3) + p_1 p_4 - p_2 p_3\right\} s^2 \\ &+ 2\hat{\omega}_p \left\{p_1 q_2 - p_2 q_1 + p_3 q_4 - p_4 q_3 + 2\hat{\omega}_p(q_1 + q_4)\right\} s. \end{aligned} \quad (14)$$

Among the transfer functions in (12), the most important factors are C_t/P_t and H_t/P_t, which explain the influence of each axis voltage to its estimated positive-sequence voltage. Therefore, these transfer functions have been crucially considered in setting the observer gains. Initially, the roll-off rate of C_t/P_t and H_t/P_t can simply be increased by setting q_1 and q_4, the highest order coefficients in the numerators, to zero

$$q_1 = q_4 = 0. \quad (15)$$

The settings of (15) are intended to enhance the filtering performance to high-frequency distortions. By (15), C_t and H_t are simplified into

$$C_t = -p_3 q_2 s^2 + 2\hat{\omega}_p p_1 q_2 s - 4\hat{\omega}_p^2 q_2 q_3 \quad (16)$$

$$H_t = -p_2 q_3 s^2 - 2\hat{\omega}_p p_4 q_3 s - 4\hat{\omega}_p^2 q_2 q_3. \quad (17)$$

To prevent nonminimum phase responses, all coefficients must have the same sign in each of (16) and (17). This condition causes the roots of each equation to be placed in the left half plane and is presented as

$$p_1/p_3 < 0 \quad q_3/p_3 > 0 \quad p_4/p_2 > 0 \quad q_2/p_2 > 0. \quad (18)$$

Meanwhile, the observer poles can be determined by using the concept of the general second-order system as follows:

$$P_{\mathrm{set}} = \left(s^2 + 2\zeta_1\omega_{n1}s + \omega_{n1}^2\right)\left(s^2 + 2\zeta_2\omega_{n2}s + \omega_{n2}^2\right) \quad (19)$$

where ζ_x is the damping ratio and ω_{nx} is the natural frequency.

After the damping ratios and natural frequencies are determined, the observer gains are set by comparing the coefficients between (14) and (19). Considering that all of the coefficients are positive in (19), the condition in (20) must be satisfied in the coefficient comparison after (15) is applied

$$p_1 + p_4 > 0 \quad q_2 q_3 < 0. \tag{20}$$

The next design point is to set the observer gains so that the observer structure is symmetric in the synchronous $d-q$ reference frame. This can contribute to the simple implementation of the observer because similar gains can be repeated in the $d-q$ reference frame, as shown in Fig. 6. The symmetric structure can be achieved with (21) when the conditions of (15), (18), and (20) are assumed

$$p_1 = p_4 \quad p_2 = -p_3 \quad q_2 = -q_3. \tag{21}$$

By the settings of (15) and (21), (13) and (14) are simplified into (22) and (23), respectively. That is, the internal transfer functions in the d-axis become similar to those in the q-axis

$$A_t = F_t = p_1 s^3 + \left\{2\hat{\omega}_p(q_2 - p_2) + p_1^2 + p_2^2\right\} s^2 + 4\hat{\omega}_p p_1 q_2 s + 4\hat{\omega}_p^2 q_2^2 \tag{22-a}$$

$$B_t = -E_t = -\left(p_2 s^3 + 2\hat{\omega}_p p_1 s^2 + 4\hat{\omega}_p^2 q_2 s\right) \tag{22-b}$$

$$C_t = H_t = p_2 q_2 s^2 + 2\hat{\omega}_p p_1 q_2 s + 4\hat{\omega}_p^2 q_2^2 \tag{22-c}$$

$$D_t = -G_t = -\left\{q_2 s^3 + p_1 q_2 s^2 + 2\hat{\omega}_p q_2 (q_2 - p_2 + 2\hat{\omega}_p) s\right\} \tag{22-d}$$

$$P_t = s^4 + 2p_1 s^3 + \left\{4\hat{\omega}_p^2 + 4\hat{\omega}_p(q_2 - p_2) + p_1^2 + p_2^2\right\} s^2 + 4\hat{\omega}_p p_1 q_2 s + 4\hat{\omega}_p^2 q_2^2. \tag{23}$$

The observer gains in (23) can then be specified with respect to predetermined damping ratios and natural frequencies in (19) by the coefficient comparison. Because harmonic distortions commonly occur at multiples of grid frequency, it would be convenient to set the natural frequency to be proportional to the grid frequency

$$\omega_{n1} = k_1 \hat{\omega}_p \quad \omega_{n2} = k_2 \hat{\omega}_p \tag{24}$$

where $\hat{\omega}_p$ is the estimated grid frequency. $\hat{\omega}_p$ has already been used for the design since (7).

For (21) and (24), the coefficient comparison between (19) and (23) results in

$$p_1 = p_4 = (\zeta_1 k_1 + \zeta_2 k_2)\hat{\omega}_p \tag{25}$$

$$4\hat{\omega}_p^2 + 4\hat{\omega}_p(q_2 - p_2) + p_1^2 + p_2^2 = \left(k_1^2 + k_2^2 + 4\zeta_1\zeta_2 k_1 k_2\right)\hat{\omega}_p^2 \tag{26}$$

$$4\hat{\omega}_p p_1 q_2 = 2k_1 k_2(\zeta_1 k_2 + \zeta_2 k_1)\hat{\omega}_p^3 \tag{27}$$

$$4\hat{\omega}_p^2 q_2^2 = k_1^2 k_2^2 \hat{\omega}_p^4. \tag{28}$$

If p_1 in (25) is inserted into (27), q_2 is uniquely determined. This resultant q_2 must then satisfy (28), which is rearranged into (29) by the substitution of the resultant q_2

$$\left(\frac{\zeta_1 k_2 + \zeta_2 k_1}{\zeta_1 k_1 + \zeta_2 k_2}\right)^2 = 1. \tag{29}$$

Because each value in (29) has been assumed to be positive, (29) is further simplified into

$$(\zeta_2 - \zeta_1)(k_1 - k_2) = 0. \tag{30}$$

When the observer poles are placed according to (19), the gain settings of (15) and (21) are used only if (30) is satisfied. One of the two factors in (30) must be zero at least for this to work. When (26) is considered in addition to (30), (31) must be satisfied if ζ_1 is equal to ζ_2, while (32) does so if k_1 is equal to k_2

$$(p_2/\hat{\omega}_p - 2)^2 = (k_1 - k_2)^2\left(1 - \zeta_1^2\right) \tag{31}$$

$$(p_2/\hat{\omega}_p - 2)^2 = -k_1^2 \cdot (\zeta_1 - \zeta_2)^2. \tag{32}$$

It is important to remember that every value is a real number in (31) and (32). According to (31), k_1 and k_2 can be different under (33)'s constraint even if ζ_1 and ζ_2 are the same. However, ζ_1 must be identical to ζ_2 in (32) if k_1 is equal to k_2. Therefore, the setting for (31) is selected to increase the degree of freedom in the observer poles

$$\left(1 - \zeta_1^2\right) \geq 0 \;\rightarrow\; -1 \leq \zeta_1 \leq 1. \tag{33}$$

In a general second-order system, oscillatory responses would occur if the damping ratio is smaller than unity. Therefore, in (33), the damping ratio could be set to unity so the observer gains in (21) are finally specified as

$$\begin{cases} p_1 = p_4 = (k_1 + k_2)\hat{\omega}_p \\ p_2 = -p_3 = 2\hat{\omega}_p \\ q_2 = -q_3 = k_1 k_2 \hat{\omega}_p / 2. \end{cases} \tag{34}$$

D. Pole Placement of the Observer

Considering (12) and (22), the estimated positive-sequence voltage is expressed by

$$\begin{cases} \hat{v}_{d+} = C_t/P_t \cdot v_d - D_t/P_t \cdot v_q \\ \hat{v}_{q+} = D_t/P_t \cdot v_d + C_t/P_t \cdot v_q. \end{cases} \tag{35}$$

The substitution of (36) makes the transfer functions similar to the general second-order system

$$k_1 = k, \quad k_2 = \rho k. \tag{36}$$

The transfer functions in (35) are then derived as (37) and (38) after reducing common factors

$$\frac{C_t}{P_t} = \frac{\rho(k\hat{\omega}_p)^2}{s^2 + (1+\rho)k\hat{\omega}_p s + \rho(k\hat{\omega}_p)^2} \tag{37}$$

$$\frac{D_t}{P_t} = -\frac{1}{2}\frac{\rho k^2 \hat{\omega}_p s}{s^2 + (1+\rho)k\hat{\omega}_p s + \rho(k\hat{\omega}_p)^2}. \tag{38}$$

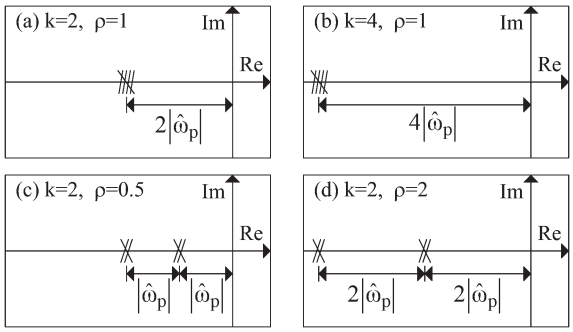

Fig. 2. Pole placements of the proposed observer according to k and ρ.

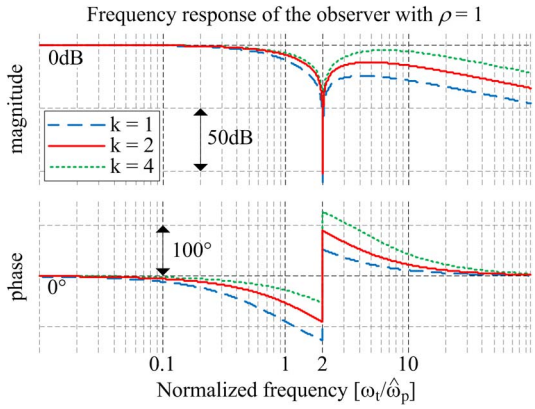

Fig. 3. Frequency response of the observer to the three-phase voltage.

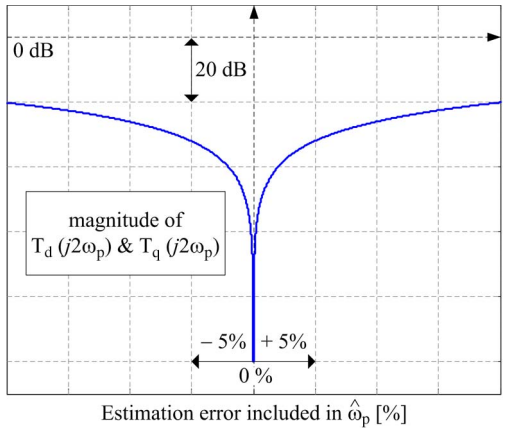

Fig. 4. Deterioration of the band-stop function by the grid frequency error.

The meaning of k and ρ can be understood from Fig. 2, where the locations of observer poles are depicted with the specific values of k and ρ. All poles are located on the negative real axis pertaining to (31) and (33). When k is set first, two poles are placed at a distance k times the grid frequency. Then, the remaining two poles are placed according to setting ρ, which is the relative distance to the first placement.

By the proposed setting in this paper, the operation of the fourth-order observer shown in (9) can be described with the second-order transfer functions in (37) and (38). This feature is very helpful in adjusting the observer responses since the original system can be understood with simple modeling. However, it is not clear what the unified effect of the proposed observer is with only (35), (37), and (38).

To analyze the unified effect, the following method is introduced based on the fact that the derived system in (8) is a linear system. Since the superposition principle holds in linear systems, the response to the three-phase voltage at each frequency can be separately considered. Considering (1) and [14], the three-phase voltage can be generalized into

$$\begin{cases} v_{ah}(t) = -V_h \sin(h\omega_p t) \\ v_{bh}(t) = -V_h \sin(h\omega_p t - 120^\circ) \\ v_{ch}(t) = -V_h \sin(h\omega_p t + 120^\circ) \end{cases} \tag{39}$$

where "h" can be any real value.

Through Park's transformation in (3), the generalized $d-q$ voltage can be derived as

$$\begin{bmatrix} v_{dh}(t) \\ v_{qh}(t) \end{bmatrix} = \begin{bmatrix} V_h \sin\left((h-1)\omega_p t\right) \\ V_h \cos\left((h-1)\omega_p t\right) \end{bmatrix} = \begin{bmatrix} V_h \sin(\omega_t t) \\ V_h \cos(\omega_t t) \end{bmatrix}. \tag{40}$$

If the Laplace transform is applied to (40), (41) is established between the d- and q-axis voltages

$$v_{dh}(s) = \frac{\omega_t}{s} v_{qh}(s). \tag{41}$$

Based on (35) and (41), the frequency response to the three-phase voltage at the arbitrary frequency, denoted by ω_t, can be derived as

$$\begin{cases} \hat{v}_{d+}(s) = \left(C_t/P_t - D_t/P_t \cdot \frac{s}{\omega_t}\right) \cdot v_{dh}(s) = T_d(s) \cdot v_{dh}(s) \\ \hat{v}_{q+}(s) = \left(D_t/P_t \cdot \frac{\omega_t}{s} + C_t/P_t\right) \cdot v_{qh}(s) = T_q(s) \cdot v_{qh}(s). \end{cases} \tag{42}$$

The Bode plot of T_d and T_q in (42) can be obtained by replacing s with $j\omega_t$ as shown in Fig. 3. Due to the symmetric design of the observer, the Bode plot of T_d is the same as that of T_q. It becomes evident how the proposed observer works in the frequency domain.

As shown in Fig. 3, the proposed observer fundamentally serves as low-pass filters in the synchronous $d-q$ reference frame while offering the band-stop function simultaneously. In particular, the bandwidth of low-pass filtering is set by the pole placement, and the stop band is located at double the estimated frequency. The low-pass function originates in the common property of the observer, while the band-stop function results from the proposed modeling of (7) to reject the negative-sequence voltage.

Although both filtering functions are affected by the estimation error of the grid frequency, the movement of the stop band is more critical. Then, it has been discussed in terms of the grid frequency error as shown in Fig. 4. When the negative-sequence voltage was considered in (42)($\omega_t = 2\omega_p$), the estimated frequency in (37) and (38) has been changed within the frequency error of 20%. As a result, even if the estimated frequency deviates from the grid frequency by 20%, the magnitude of the negative-sequence voltage is still expected to be mitigated by the observer by up to one-tenth.

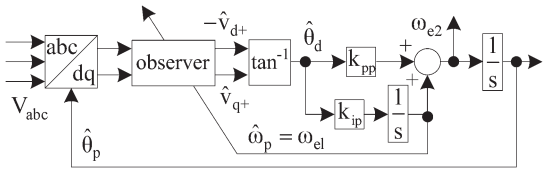

Fig. 5. Entire PLL structure.

III. PLL Based on the Observer

The observer proposed in Section II is attached to SRF-PLL. By virtue of this construction, filtering harmonics can be readily achieved with less effort in PLL, which allows PLL to increase its bandwidth and contributes to the higher phase-angle tracking dynamics. The entire PLL structure is shown in Fig. 5 and is referred to as synchronous observer-aided preprocessing PLL (SOAP-PLL).

The estimated frequency in PLL must be fed back to set the observer gains according to (34). Usually, ω_{e2} in Fig. 5 has been used as the estimated frequency. However, ω_{e2} may be sensitive to distortions because k_{pp}, the proportional gain, directly delivers scaled angle errors to it. To refine this drawback, ω_{e1} in Fig. 5 is used as the estimated grid frequency. The effectiveness of this modification can be discussed with the following equations. When (43) is assumed, (44) can be derived from Fig. 5

$$\hat{\theta}_d \approx \theta_d = \theta_p - \hat{\theta}_p \tag{43}$$

$$\hat{\theta}_p = \frac{k_{pp}s + k_{ip}}{s^2 + k_{pp}s + k_{ip}}\,\theta_p \tag{44}$$

where k_{pp} and k_{ip} are proportional and integral (PI) gains for PLL, respectively.

From Fig. 5 with (43), ω_{e1} is derived as

$$\omega_{e1} = \frac{k_{ip}}{s}\,\hat{\theta}_d \approx \frac{k_{ip}}{s}(\theta_p - \hat{\theta}_p). \tag{45}$$

If $\hat{\theta}_p$ in (44) is inserted into (45), it can be rearranged into

$$\omega_{e1} \approx \frac{k_{ip}s}{s^2 + k_{pp}s + k_{ip}}\,\theta_p = \frac{k_{ip}}{s^2 + k_{pp}s + k_{ip}}\,\omega_p. \tag{46}$$

ω_{e1} is a low-pass-filtered value of the actual frequency. By using this frequency as $\hat{\omega}_p$, the observer performance can be less sensitive to distortions. In addition, because the transfer function in (46) takes the form of the general second-order system, the PI gains can be set according to the setting rules of the second-order system

$$k_{pp} = 2\zeta_{\mathrm{pll}}\omega_{\mathrm{npll}}, \quad k_{ip} = \omega_{\mathrm{npll}}^2 \tag{47}$$

where ζ_{pll} and ω_{npll} are the damping ratio and natural frequency of PLL, respectively.

The gain settings of the observer and PLL have to come together, so all the gains are set where the bandwidth of (37) is larger than that of (44). Empirically, the bandwidth of (37) is set to four times greater than that of (44). If the dominant pole of the observer is not larger than that of PLL, the dynamics intended in (44) would be disturbed.

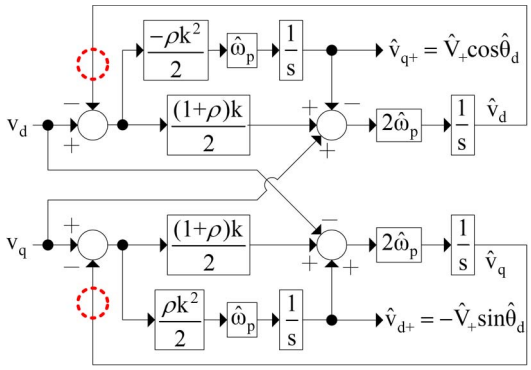

Fig. 6. Block diagram of the proposed observer.

Meanwhile, based on the equation obtained from dividing both sides of (10) by "s," the proposed observer can be specifically implemented, as shown in Fig. 6. In the process of obtaining Fig. 6, the observer gains have been set according to (15), (34), and (36). Even though the observer design seems to be rather complicated, the practical implementation of the proposed observer is simple. As discussed earlier, this single observer can offer the low-pass and band-stop functions simultaneously.

IV. Simulation and Experimental Results

A. Evaluation of SOAP-PLL

The performance of SOAP-PLL can be discussed in two aspects: the tracking error on grid parameters and the mitigating ability against distortions. Each performance has been examined under grid faults where the grid voltages were contaminated by harmonics and unbalances, and the grid frequency was changed.

In particular, the effectiveness of SOAP-PLL is discussed as compared to DSOGI-FLL. This method has been selected because its implementation is relatively simple, and essential gain settings are known [10].

B. Simulation Results

The fault conditions for the simulation tests have been quoted from the literature [12]. When the voltage amplitude at an ideal grid is selected as the base voltage, the phasor of the normal voltage is denoted as $1\angle 0°$. Based on this concept, the fault conditions are given as follows:

$$V_{1+} = 0.5\angle -30° \quad V_{1-} = 0.25\angle 110° \tag{48}$$

$$V_{5-} = 0.2\angle 0° \quad V_{7+} = 0.2\angle 0° \quad V_{11-} = 0.2\angle 0° \tag{49}$$

$$f_{\mathrm{fault}} - f_{\mathrm{nor}} = -5\ \mathrm{Hz} \tag{50}$$

where the subscript number of a voltage represents harmonic order and the normal condition is indicated by the subscript "nor."

When the normal grid is assumed to be 220 V_{rms}–60 Hz and all of the conditions in (48)–(50) are applied after the fault, the fault waveforms are shown in Fig. 7.

Initially, the gains of DSOGI-FLL were set according to earlier work [10]. For a fair comparison of performances, the gains of SOAP-PLL had to be set such that its dynamics were

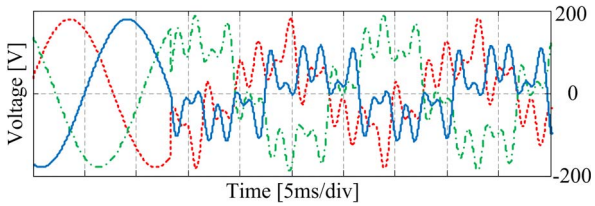

Fig. 7. Grid fault under the conditions of (48)–(50).

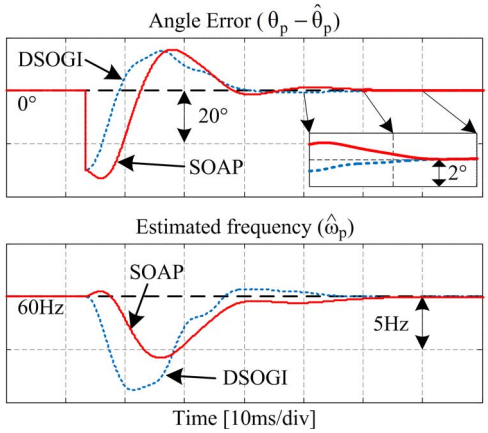

Fig. 8. Simulation results under the unbalance fault of (48) with analog implementations.

similar to those of DSOGI-FLL under the unbalance fault of (48). The specific values of those gains were

$$\rho = 1 \quad k = 1.7 \quad \zeta_{\text{pll}} = 1 \quad \omega_{\text{npll}} = 2\pi \cdot 20. \tag{51}$$

The gains of ρ and k are directly inserted into the observer of Fig. 6, and the gains of ζ_{pll} and ω_{npll} are reflected in the PLL of Fig. 5 through the PI gains in (47). With these specific values, SOAP-PLL has presented the same settling time under the condition specified in (48), as shown in Fig. 8.

Due to the step variations in (48), the estimation errors of the phase angle and frequency present oscillations for a while after the fault, as captured in Fig. 8. However, after the oscillations disappear, both methods shows perfect grid synchronizations as if there are no unbalance distortions, which confirms that the unbalance rejection of SOAP-PLL is comparable with that of DSOGI-FLL.

The performance of SOAP-PLL was different to that of DSOGI-FLL when each method was implemented in a discrete time domain, or the harmonics in (49) were included in fault conditions. The digital implementation of DSOGI-FLL was based on [21], while SOAP-PLL was simply implemented with backward Euler method. With these implementations under 10-kHz samplings, each method was tested under the fault conditions of (48)–(50). The simulation result is presented in Fig. 9.

As shown in Fig. 9, SOAP-PLL obviously outperforms DSOGI-FLL in harmonic filtering. This is because SOAP-PLL consists of two filtering stages: the observer and the PLL. Even though the filtering performance of DSOGI-FLL can be improved by extending to multiple SOGI-FLL [12], this extension can only be done by increasing the source code lines for implementation. In addition, the frequency of DSOGI-FLL presents the average error of 0.79 Hz mainly due to harmonics.

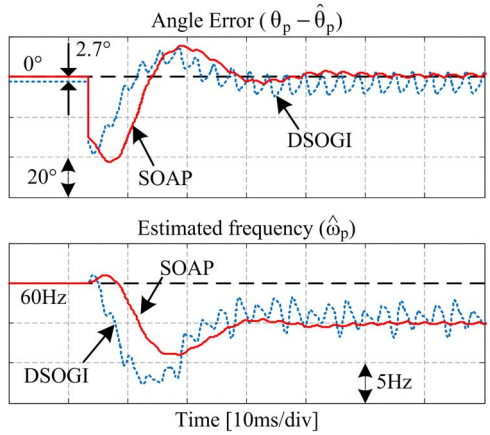

Fig. 9. Simulation results under the fault conditions of (48)–(50) with digital implementations.

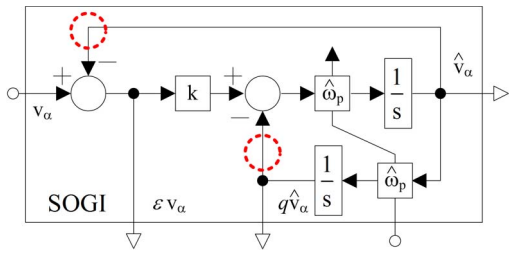

Fig. 10. Second-order generalized integrator.

The other conspicuous feature is that DSOGI-FLL shows the steady-state error of 2.7° in estimating the phase angle. To discuss this phenomenon, one of the dual SOGIs is shown in Fig. 10. To estimate the positive-sequence voltage, the following transfer functions are important in Fig. 10:

$$D(s) = \frac{k\hat{\omega}_p s}{s^2 + k\hat{\omega}_p s + \hat{\omega}_p^2} = \frac{\hat{v}_\alpha}{v_\alpha} \tag{52-a}$$

$$Q(s) = \frac{k\hat{\omega}_p^2}{s^2 + k\hat{\omega}_p s + \hat{\omega}_p^2} = \frac{q\hat{v}_\alpha}{v_\alpha} \tag{52-b}$$

where the subscript "α" refers to the d-axis in the stationary reference frame. $Q(s)$ particularly generates the quadrature signal of the input, while both $D(s)$ and $Q(s)$ serve as filtering harmonics.

When a system is transformed from the s-domain to the z-domain, its original property can be distorted. Moreover, the computational delay of z^{-1}, which is indicated by dashed circles in Figs. 6 and 10, may be included for feedback. To specify these types of distortions, the z-transformation distortion (ZTD) is introduced

$$\text{ZTD}_H(\omega) = \frac{H_z(e^{j\omega T_s})}{H_s(j\omega)} \tag{53}$$

where "H" symbolizes the system of interest, H_s refers to the original system in the s-domain, and H_z represents the transformed system in the z-domain. In addition, ω is the frequency of concern, and T_s is the sampling period for digital implementation.

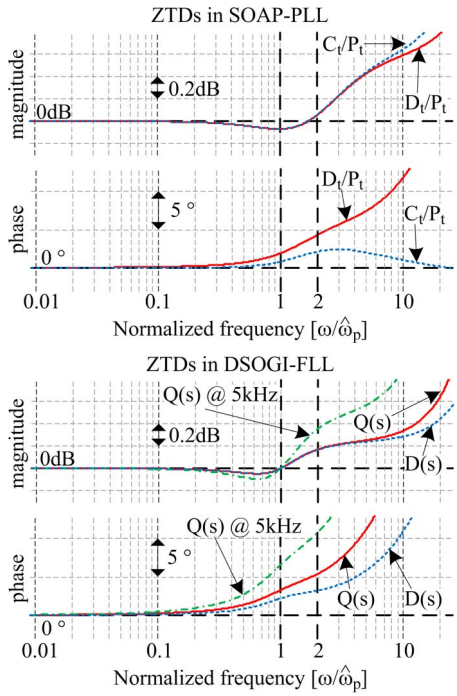

Fig. 11. Bode plots of ZTDs in SOAP-PLL and DSOGI-FLL under 10-kHz samplings.

The meaning of ZTD is the distorted degree of the z-domain system from the s-domain system. The Bode plot of ZTD corresponds to the differences between the Bode plots of each system

$$20\log_{10}|\mathrm{ZTD}_H(\omega)| = 20\log_{10}\left|H_z(e^{j\omega T_s})\right| - 20\log_{10}|H_s(j\omega)| \quad (54)$$

$$\angle\mathrm{ZTD}_H(\omega) = \angle H_z(e^{j\omega T_s}) - \angle H_s(j\omega). \quad (55)$$

The Bode plots of critical ZTDs in SOAP-PLL and DSOGI-FLL are depicted in Fig. 11, where the sampling frequency is set at 10 kHz. In the Bode plot of ZTD, magnitude and phase must be 0 dB and 0°, respectively, which correspond to unity, when the z-transformation is ideal. As shown in Fig. 11, the ZTDs deviate from the unity when the frequency of concern approaches the Nyquist frequency.

From Fig. 11, the reason for the steady-state error in DSOGI-FLL and not in SOAP-PLL can be explained. SOAP-PLL and DSOGI-FLL are different theoretically since SOAP-PLL can separate the positive- and negative-sequence voltages via Park's transformation. By this separation, the negative-sequence voltage appears at double the grid frequency, while the positive-sequence voltage is at the dc band. In contrast, DSOGI-FLL deals with the positive- and negative-sequence voltages in the stationary reference frame, where both voltages appear at the grid frequency.

As shown in Fig. 11, the ZTDs of $D(s)$ and $Q(s)$ in (52) exhibit the phase distortions of 2.2 and 3.2° at the grid frequency, where the positive-sequence voltage appears in DSOGI-FLL. For ac signals, these nonzero phases mean parallel displacements in the time domain. Then, the phase distortion of the positive-sequence voltage can cause the steady-state error in DSOGI-FLL and can be intensified at smaller sampling frequencies as shown in Fig. 11 (denoted by @5 kHz). In contrast, the ZTDs of SOAP-PLL present almost unity at the dc band, where the positive-sequence voltage appears in SOAP-PLL. In other words, the positive-sequence voltage would not be distorted in SOAP-PLL. Although the observer function is slightly distorted at double the grid frequency as shown in Fig. 11, the effectiveness of the band-stop function in SOAP-PLL can be corroborated with the result of Fig. 9. Unlike SOAP-PLL, careful considerations are required for digital implementation of DSOGI-FLL [20]–[22].

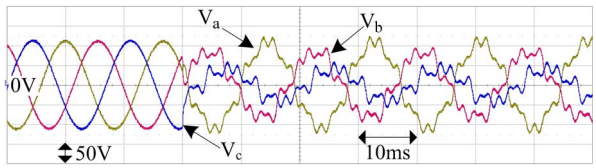

Fig. 12. Grid fault for experiment.

In addition, the condition of (50) has also been included in the fault test of Fig. 9 to examine the frequency-adaptive property of SOAP-PLL. Because the second-order distortions are not observed often in Fig. 9, the SOAP-PLL successfully rejects the negative-sequence voltage even after frequency variation.

C. Experimental Results

To demonstrate the feasibility of SOAP-PLL, a grid fault was emulated using an ac programmable source, MX30. All algorithms were implemented in a digital signal processor (DSP), TMS320F28335, and grid voltages were sampled through voltage sensors per 100 μs. All of the gains for SOAP-PLL were set according to (51).

The most frequent fault is the single phase-to-ground fault [17], which is commonly recognized as phase-to-phase fault by grid-connected converters due to transformers [19]. The phase-to-phase fault between b- and c-phases has been considered

$$\begin{cases} V_a = 1 \\ V_b = -1/2 - jV_{\mathrm{sag}}\sqrt{3}/2 \\ V_c = -1/2 + jV_{\mathrm{sag}}\sqrt{3}/2 \end{cases} \quad (56)$$

where V_{sag} is a complex number indicating the degree of voltage sag. In addition, all magnitudes are in per unit.

The magnitude of V_{sag} is determined according to the phase of V_{sag}[19]. As an experiment, V_{sag} was set to $0.38\angle -40°$. The magnitudes of harmonics at 5th, 7th, and 11th orders were set to about 0.08 per unit, and the frequency variation in (50) was included as well. The grid voltages around the fault occurrence are shown in Fig. 12, which are the voltages recognized by the DSP board.

Initially, the c-phase voltage, whose negative peak was the starting point of the fault, was selected as the reference signal to capture several waveforms from the limited channels of the oscilloscope. It was assumed that the ac source could generate almost time-invariant faults according to the same settings.

Under the fault situation, SOAP-PLL has the fewest harmonics in the frequency estimation shown in Fig. 13. The effect of the proposed observer can be more obvious via the comparison with SRF-PLL, where only the observer part has been

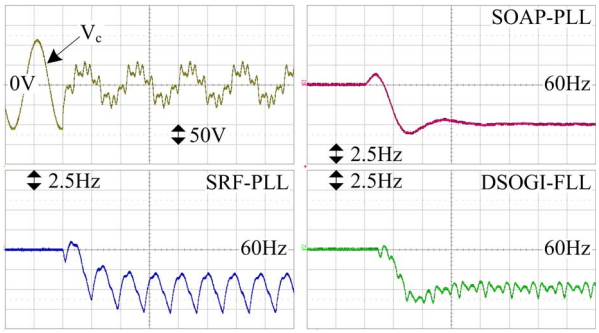

Fig. 13. Frequency estimations in the experiment: time (10 ms/div).

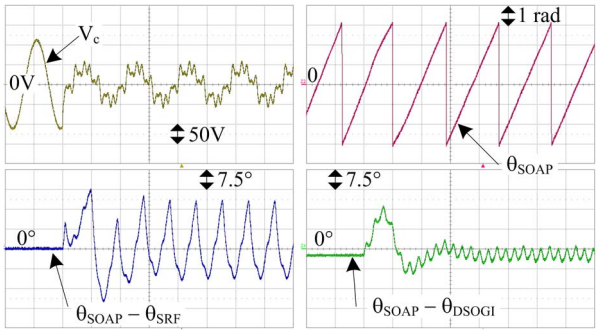

Fig. 14. Angle estimations in the experiment: time (10 ms/div).

eliminated from SOAP-PLL. As shown in Fig. 13, negative-sequence distortions were evidently rejected by SOAP-PLL when compared with SRF-PLL. After transient situations, the rms of the frequency ripple was 0.1 Hz for SOAP-PLL, 1.52 Hz for SRF-PLL, and 0.45 Hz for DSOGI-FLL. Furthermore, the frequency of DSOGI-FLL presented the average deviation of 0.102 Hz when compared to SOAP-PLL.

Because the actual phase angle was not accessed, angle errors were calculated with respect to the phase angle of SOAP-PLL θ_{SOAP} when considering the simulation result. After transient situations, the phase angle of DSOGI-FLL θ_{DSOGI} deviated from that of SOAP-PLL by 2.4°, as shown in Fig. 14.

V. Conclusion

In this paper, an observer has been proposed to clearly extract the positive-sequence voltage from the polluted grid voltage. This extraction is intended to reinforce the function of PLL by using the observer as a preprocessor. The state equation has been newly derived on grid voltage to construct the observer, and the gain settings of the observer have been suggested when considering the mitigation of grid distortions and their combination with PLL.

In a functional aspect, the proposed PLL method has been specifically scrutinized in terms of filtering harmonics and rejecting unbalances under polluted grid conditions. In particular, the performances have been discussed in digitally implemented structures under the consideration of practical implementation. As a result, the effectiveness of the proposed method has been confirmed by simulation and experimental results. The proposed method excelled in mitigating distortions of the estimated frequency and phase angle without steady-state errors.

References

[1] A. E. Emanuel, "Summary of IEEE Standard 1459: Definitions for the measurement of electric power quantities under sinusoidal, nonsinusoidal, balanced, or unbalanced conditions," *IEEE Trans. Ind. Appl.*, vol. 40, no. 3, pp. 869–876, May/Jun. 2004.

[2] V. Kaura and V. Blasko, "Operation of a phase locked loop system under distorted utility conditions," *IEEE Trans. Ind. Appl.*, vol. 33, no. 1, pp. 58–63, Jan./Feb. 1997.

[3] S.-K. Chung, "A phase tracking system for three phase utility interface inverters," *IEEE Trans. Power Electron.*, vol. 15, no. 3, pp. 431–438, May 2000.

[4] S.-J. Lee, H. Kim, and S.-K. Sul, "A new phase detecting method for power conversion systems considering distorted conditions in power system," in *Conf. Rec. 34th IEEE IAS Annu. Meeting*, Oct. 3–7, 1999, pp. 2167–2172.

[5] R. K. Sinha and P. Sensarma, "A pre-filter based PLL for three-phase grid connected applications," *Elect. Power Syst. Res.*, vol. 81, no. 1, pp. 129–137, Jan. 2011.

[6] M. P. Kazmierkowski, M. Jasinski, and G. Wrona, "DSP-based control of grid-connected power converters operating under grid distortions," *IEEE Trans. Ind. Informat.*, vol. 7, no. 2, pp. 204–211, May 2011.

[7] F. Liccardo, P. Marino, and G. Raimondo, "Robust and fast three-phase PLL tracking system," *IEEE Trans. Ind. Electron.*, vol. 58, no. 1, pp. 221–231, Jan 2011.

[8] F. Gonzalez-Espin, E. Figueres, and G. Garcera, "An adaptive synchronous-reference-frame phase-locked loop for power quality improvement in a polluted utility grid," *IEEE Trans. Ind. Electron.*, vol. 59, no. 6, pp. 2718–2731, Jun. 2012.

[9] Y. F. Wang and Y. W. Li, "Grid synchronization PLL based on cascaded delayed signal cancellation," *IEEE Trans. Power Electron.*, vol. 26, no. 7, pp. 1987–1997, Jul. 2011.

[10] P. Rodriguez, A. Luna, R. S. Munoz-Aguilar, I. Etxeberria-Otadui, R. Teodorescu, and F. Blaabjerg, "A stationary reference frame grid synchronization system for three-phase grid-connected power converters under adverse grid conditions," *IEEE Trans. Power Electron.*, vol. 27, no. 1, pp. 99–122, Jan. 2012.

[11] P. Rodriguez, J. Pou, J. Bergas, J. I. Candela, R. P. Burgos, and D. Boroyevich, "Decoupled double synchronous reference frame PLL for power converters control," *IEEE Trans. Power Electron.*, vol. 22, no. 2, pp. 584–592, Mar. 2007.

[12] P. Rodriguez, A. Luna, I. Candela, R. Mujal, R. Teodorescu, and F. Blaabjerg, "Multiresonant frequency-locked loop for grid synchronization of power converters under distorted grid conditions," *IEEE Trans. Ind. Electron.*, vol. 58, no. 1, pp. 127–138, Jan. 2011.

[13] X. Guo, W. Wu, and Z. Chen, "Multiple-complex coefficient-filter-based phase-locked loop and synchronization technique for three-phase grid-interfaced converters in distributed utility networks," *IEEE Trans. Ind. Electron.*, vol. 58, no. 4, pp. 1194–1204, Apr. 2011.

[14] E. Robles, S. Ceballos, J. Pou, J. L. Martin, J. Zaragoza, and P. Ibanez, "Variable-frequency grid-sequence detector based on a quasi-ideal low-pass filter stage and a phase-locked loop," *IEEE Trans. Power Electron.*, vol. 25, no. 10, pp. 2552–2563, Oct. 2010.

[15] I. Carugati, S. Maestri, P. G. Donato, D. Carrica, and M. Benedetti, "Variable sampling period filter PLL for distorted three-phase systems," *IEEE Trans. Power Electron.*, vol. 27, no. 1, pp. 321–330, Jan. 2012.

[16] D. G. Luenberger, "An introduction to observers," *IEEE Trans. Autom. Control*, vol. AC-16, no. 6, pp. 596–602, Dec. 1971.

[17] J. Keller and B. Kroposki, "Understanding fault characteristics of inverter-based distributed energy resources," NREL, Golden, CO, USA, Tech. Rep. NREL/TP-550-46698, Jan. 2010.

[18] A. R. Bergen and V. Vittal, "Symmetrical components," in *Power Systems Analysis*, 2nd ed. Seoul, Korea: Pearson Educ. Korea Ltd, 2009, ch. 12-1, pp. 446–450.

[19] A. Sannino, M. H. J. Bollen, and J. Svensson, "Voltage tolerance testing of three-phase voltage source converters," *IEEE Trans. Power Del.*, vol. 20, no. 2, pp. 1633–1639, Apr. 2005.

[20] A. G. Yepes, F. D. Freijedo, J. Doval-Gandoy, O. Lopez, J. Malvar, and P. Fernandez-Comesana, "Effects of discretization methods on the performance of resonant controllers," *IEEE Trans. Power Electron.*, vol. 25, no. 7, pp. 1692–1712, Jul. 2010.

[21] F. J. Rodriguez, E. Bueno, M. Aredes, L. G. B. Rolim, F. A. S. Neves, and M. C. Cavalcanti, "Discrete-time implementation of second order generalized integrators for grid converters," in *Proc. IEEE IECON*, Nov. 10–13, 2008, pp. 176–181.

[22] A. G. Yepes, F. D. FreiJedo, O. Lopez, and J. Doval-Gandoy, "High-performance digital resonant controllers implemented with two integrators," *IEEE Trans. Power Electron.*, vol. 26, no. 2, pp. 563–576, Feb. 2011.

Yongsoon Park (S'12) received the B.S. and M.S. degrees in electrical engineering from Seoul National University, Seoul, Korea, in 2008 and 2010, respectively, where he is currently working toward the Ph.D. degree.

His current research interests are sensorless drives of electrical machines and power conversion circuits.

Seung-Ki Sul (S'78–M'80–SM'98–F'00) received the B.S., M.S., and Ph.D. degrees in electrical engineering from Seoul National University, Seoul, Korea, in 1980, 1983, and 1986, respectively.

From 1986 to 1988, he was an Associate Researcher with the Department of Electrical and Computer Engineering, University of Wisconsin, Madison, WI, USA. From 1988 to 1990, he was a Principal Research Engineer with Gold-Star Industrial Systems Company. Since 1991, he has been a member of the faculty of the School of Electrical Engineering, Seoul National University, where he is currently a Professor. From 2005 to 2007, he was the Vice Dean of the Engineering College with Seoul National University. From 2008 to 2011, he was the President of the Korea Electrical Engineering and Science Research Institute (KESRI), Seoul. His current research interests are power electronic control of electrical machines, electric/hybrid vehicle and ship drives, and power converter circuits.

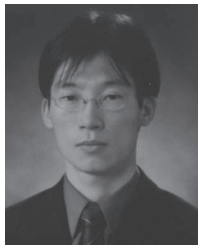

Woo-Chull Kim was born in Korea in 1976. He received the B.S. degree in information and communication engineering from Suwon University, Suwon, Korea, in 2003.

Since 2011, he has been a Research Engineer with LG Uplus, Inc., Seoul, Korea. His current research interests include power electronic control of renewable energy.

Hyun-Young Lee received the M.S.E.E. degree from Ulsan University, Ulsan, Korea, in 2004.

He is currently a Senior Electrical Engineer with PLASPO Company, Ltd., Goyang City, Korea. His research interests include power electronics, motor controls, soft switching, photovoltaic systems, and communication techniques.